

Ground-based, daytime modeling and observations in SWIR for satellite custody

Grant M. Thomas

Air Force Institute of Technology, Wright-Patterson AFB, Ohio

Richard G. Cobb

Air Force Institute of Technology, Wright-Patterson AFB, Ohio

ABSTRACT

Space Situational Awareness (SSA) can be summarized as the ability to monitor, understand and predict natural and man-made resident space objects. At each ground sensor location, gaps in custody emerge as dim objects fall below detectability thresholds with the rising Sun. The length of the custody-gap for a particular satellite depends on the apparent brightness of that satellite and the brightness of the sky background within the field-of-view at the time of observation. Since daytime skies are slightly darker in the infrared, low-cost, passive SWIR sensors are a viable solution for daytime satellite detection. This research develops and validates models of the daytime sky spectral radiance to compare to custody observations in the near-infrared (NIR) and short-wave infrared (SWIR) wavelengths. Sky radiance model accuracy is quantified via observations from three test campaigns with spectral, temporal, spatial-pointing, and ground-site diversity. Ground-level, in-situ measurements of aerosol particles and meteorological inputs significantly increase the accuracy of sky radiance models. Lastly, the efficacy of SWIR daytime custody is demonstrated via a series of exo-atmospheric target observations in the daytime sky quantifying the performance and limitations of utilizing low-cost, SWIR sensors in accomplishment of the ground-based, daytime custody mission.

1 INTRODUCTION

Accurate daytime sky radiance modeling in the Near-Infrared (NIR) and Short-Wave Infrared (SWIR) spectral bands is critical for emerging technologies such as daytime satellite custody and tracking, and quantum-key distribution where noisy backgrounds affect detectable signals and limit anticipated utility. The spectral radiance of the daytime sky is dependent on the time of day, season, atmospheric constituents and local conditions. These conditions are in a state of constant fluctuation and may cause the spectral radiance of the sky to vary greatly from day to day. The direct solar radiation coming to Earth from the Sun is attenuated by the atmospheric absorption and scattering. Sunlight interacts with atmospheric particles and molecules through single and multiple scattering processes resulting in some amount of spectral radiance coming out of all parts of the sky whether cloudy or clear [22]. This detectable sky brightness can be separated into diffuse and direct components which are primarily a function of two mechanisms: scattered radiation from the Sun and emission by atmospheric constituents [1]. However, for visible through SWIR wavelengths, scattering is critical and is the primary loss mechanism considered in this analysis. Molecular scattering effects are directly proportional to λ^{-4} with the net result that blue light is scattered more than red light, and the sky is increasingly darker in the infrared. Quantifying the anticipated spectral radiance in the I- and J-bands ($\sim 0.8\mu\text{m}$ and $\sim 1.2\mu\text{m}$ respectively) is the focus of this study. While not exhaustive, quantification of this data subset indicates the model trends and reinforces the importance of aerosol content scaling to more accurately characterize the aerosol profile effects on sky radiance predictions. This research relies on the Laser Environmental Effects Definition and Reference (LEEDR) [10] model to propagate scattered light from the Sun through the atmosphere and to the sensor.

LEEDR is an atmospheric characterization and radiative transfer code that calculates line-by-line (point-wise solutions for specific wavelengths) and spectral band solutions by creating “correlated, physically realizable profiles of meteorological and environmental effects (e.g. gaseous and particle extinction, optical turbulence, and cloud free line of sight) data” [7]. LEEDR is favored over the Moderate Resolution Atmospheric Transmission (MODTRAN) [3] model as LEEDR is better suited to ingest volumetric numerical weather prediction models and scale the boundary layer and aerosol loading with ground-based measurements. LEEDR has the ability to generate realistic atmospheric profiles from probabilistic climatology or observations and forecasts from numerical weather prediction models and atmospheric attenuation models. LEEDR makes radiative transfer calculations based on inputs that closely mirror the atmospheric conditions on a given date, time, and location thus provide more realistic approximation of the spectral sky radiance and atmospheric transmission than what could be obtained with inputs based solely on atmospheres [20]. Accurate results are possible by capturing the dominant radiometric transfer physics and atmospheric attenuation of each layer. As part of LEEDR’s verification and validation Burley [4] made comparisons of LEEDR’s calculated sky radiances against measurements in Germany in 2012 [19].

Both LEEDR and MODTRAN model the spectral sky radiance by propagating the radiance of the near-blackbody radiation of the Sun through multiple layers of distinct homogeneous atmosphere. The atmospheric layers are characterized by a fixed temperature, pressure, and molecular constituency [2]. By sequencing subsequent layers where the exiting irradiance of the previous layer becomes the entering radiance of the next, the total effective radiance is readily calculated as in Figure 1.

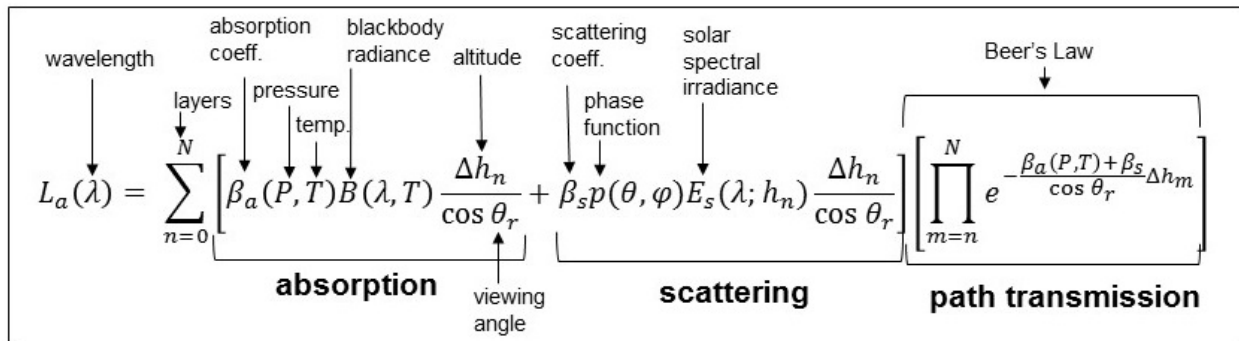


Figure 1: Atmospheric path radiance from object to sensor [9]

Thus the spectral radiance may be calculated for each atmospheric layer as a function of meteorology (temperature, pressure, humidity), aerosol loading (scattering, absorption), and optical depth as shown in Figure 1. Atmospheric layers may be combined to determine the total atmospheric scattering effects and transmission losses along the radiative path.

2 APPROACH

2.1 Custody-Gap Modeling and Analysis from SOR Measurements

Daytime imaging of satellites is challenging due to the changing sky background and the fluctuation of the received satellite signal depending on satellite pose relative the observer, surface area and material reflectance properties. The received photometric intensity is far from constant and is difficult to model even knowing the orientation of the satellite such as in GEO orbit. However stars, unlike satellite targets, have constant flux. By selecting a star with flux intensity near that of a LEO satellite ($\sim 4-6$ visual magnitude) this research was able to compare the impact of increasing sky brightness on a target with constant magnitude [15].

2.1.1 Star Selection and Measurement

Hipparcos catalog (HIP) star 16489 is a G5-series star which has an approximate temperature, T , of 5620K [14]. From Wein’s law, the wavelengths of peak spectral radiance, λ_{peak} , of the Sun and HIP 16489

may be calculated as in Equation 1 and are shown in Table 1.

$$\lambda_{peak} = \frac{2898}{T} \quad (1)$$

Table 1: Wavelength of peak spectral radiance for our Sun and HIP 16489.

Object	Spectral Class	Temp. [K]	λ_{peak} [m]
Sun	G2	5800	0.4997
HIP 16489	G5	5620	0.5157

Satellite signals are often more reflective in the infrared bands than in the visible bands due to the reflectance profile of the solar arrays [6]. Thus HIP 16489, with slightly red-shifted peak wavelength intensity, is a realistic proxy for a satellite that is reflecting the Sun's radiance. The filter passbands and catalog visual magnitudes for HIP 16489 are shown in Figure 2. Catalog filters referenced are Johnson-B and V [13], Cousins-I [17], and 2MASS J, H, and Ks [8].

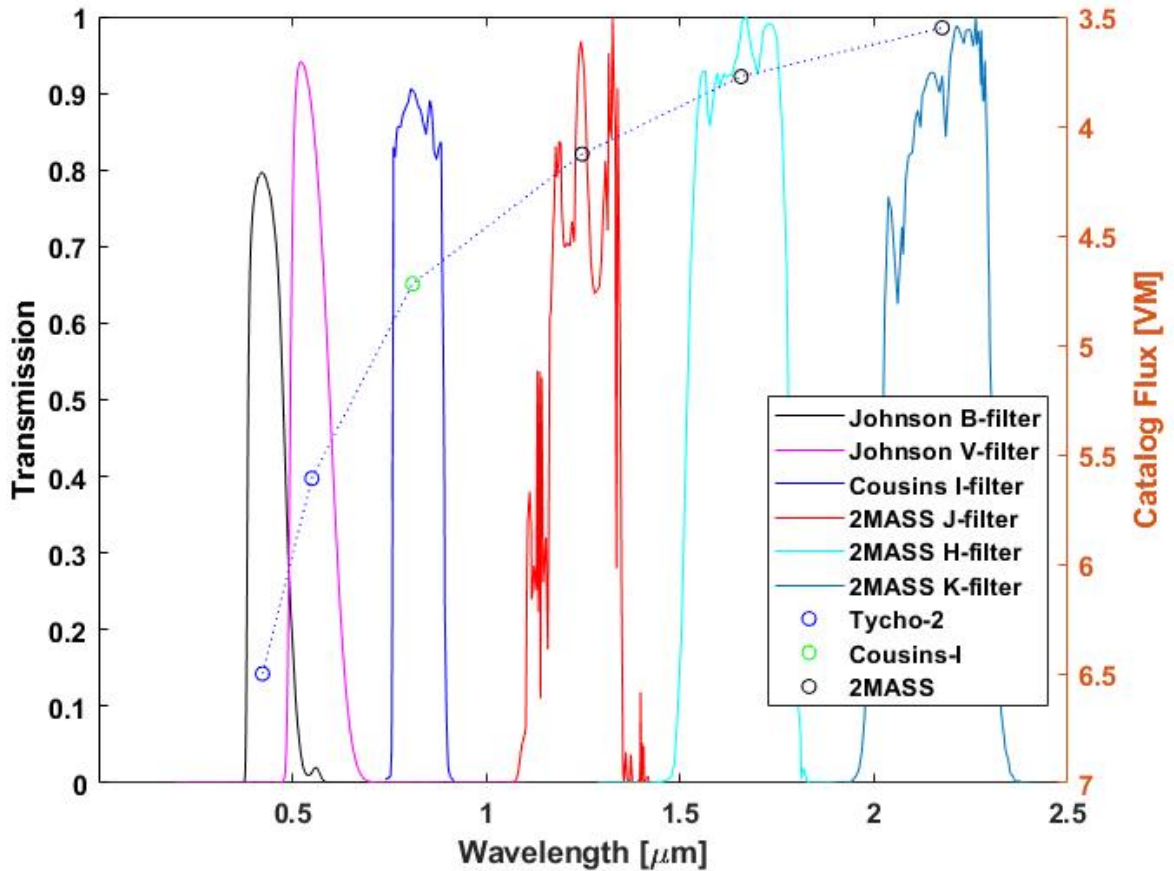


Figure 2: Catalog filter passbands and catalog flux for HIP 16489

On 18 Mar 19, HIP 16489 was observed approximately every 15 mins from 1230 – 1730 UTC (0630L – 1130L) from the Starfire Optical Range at Kirtland AFB, NM. The azimuths ranged from 2-6°N and elevations of 30-34° measured from the local horizon during the observation period. Sunrise occurred at 1313 UTC (0713L) for that date. Sample images of the data collection are shown in Figure 4 for the I- and J-band cameras as well as the all-sky camera in Figure 3. The approximate observed position of the star for each given time is shown as a red-dot on the all-sky camera image for each time step in Figure 3.

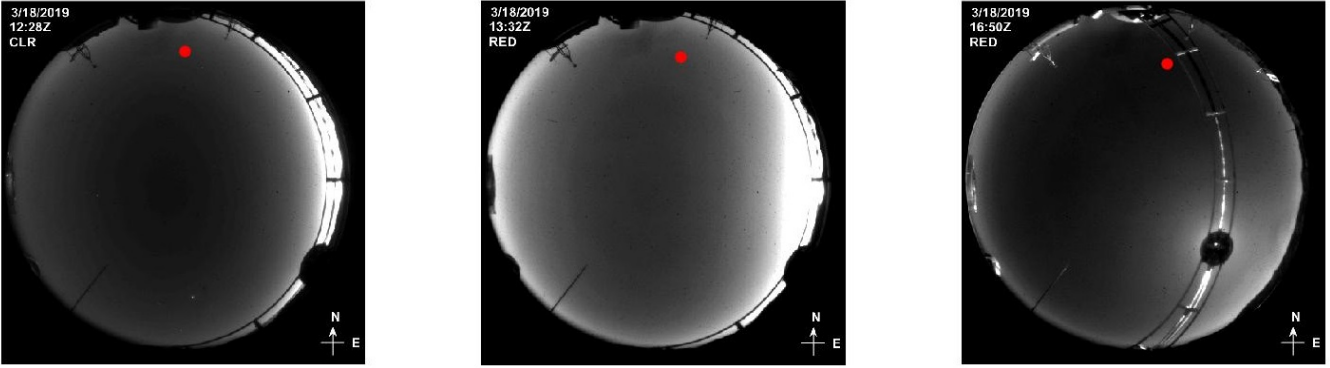


Figure 3: All-sky images from SOR during observation window at approximately 1228, 1330, and 1650 UTC. HIP 16489 observation location shown as a red-dot on each respective image. The azimuths ranged from 2-6°N and elevations of 30-34° measured from the local horizon during the observation period. Sunrise occurred at 1313 UTC for that date.

Each image of HIP 16489 may be processed to determine the OSR of an image. Since the point-spread function (PSF) of the star is spread across multiple pixels, only consider the OSR of the brightest pixel is considered [11]. The I- and J-band OSRs for the 18 Mar 19, HIP 16489 observations from 1230 – 1730 UTC (0630L – 1130L) from the Starfire Optical Range at Kirtland AFB, NM are shown in Figure 4. The observation azimuths ranged from 2-6°N and elevations of 30-34° measured from the local horizon during the observation period. During periods of low mean sky background, the OSR for the I-band camera significantly exceeds that of the J-band camera. However, as the sky background intensity increases, higher OSRs in the J-band are observed.

Assuming that higher OSRs enable higher mission success rates of the custody mission, Figure 5 implies that a shift from I- to J-band custody should occur when the mean sky background $\sim 3E6$ ADUs (aka counts) to maintain custody with the highest possible OSR.

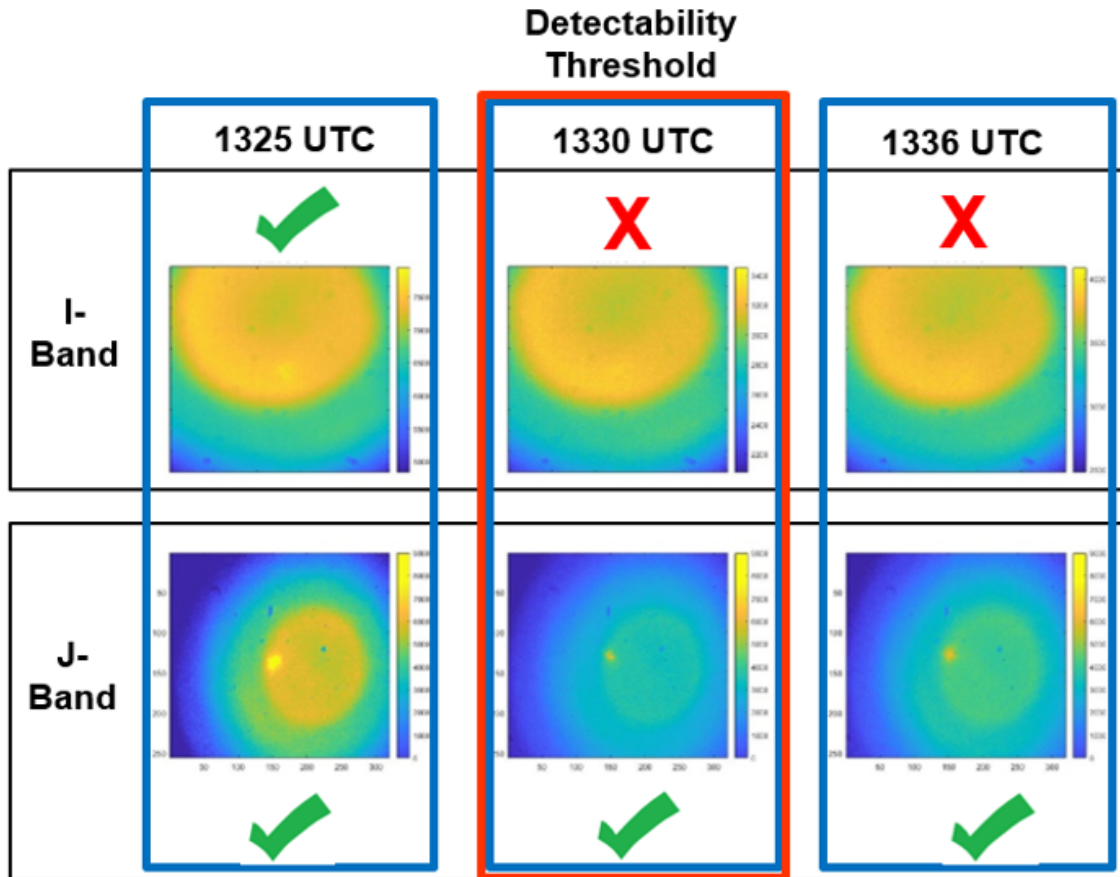


Figure 4: Sample images of the 18 Mar 19, HIP 16489 observations for the I- and J-band cameras (top and bottom rows respectively) from the SOR at Kirtland AFB, NM near the observed I-band detectability threshold. I-band OSR at detectability threshold was observed to be 0.0032 at 1330 UTC (0730L). HIP 16489 catalog fluxes are: 4.72 (I-band) and 4.13 (J-band) [14].

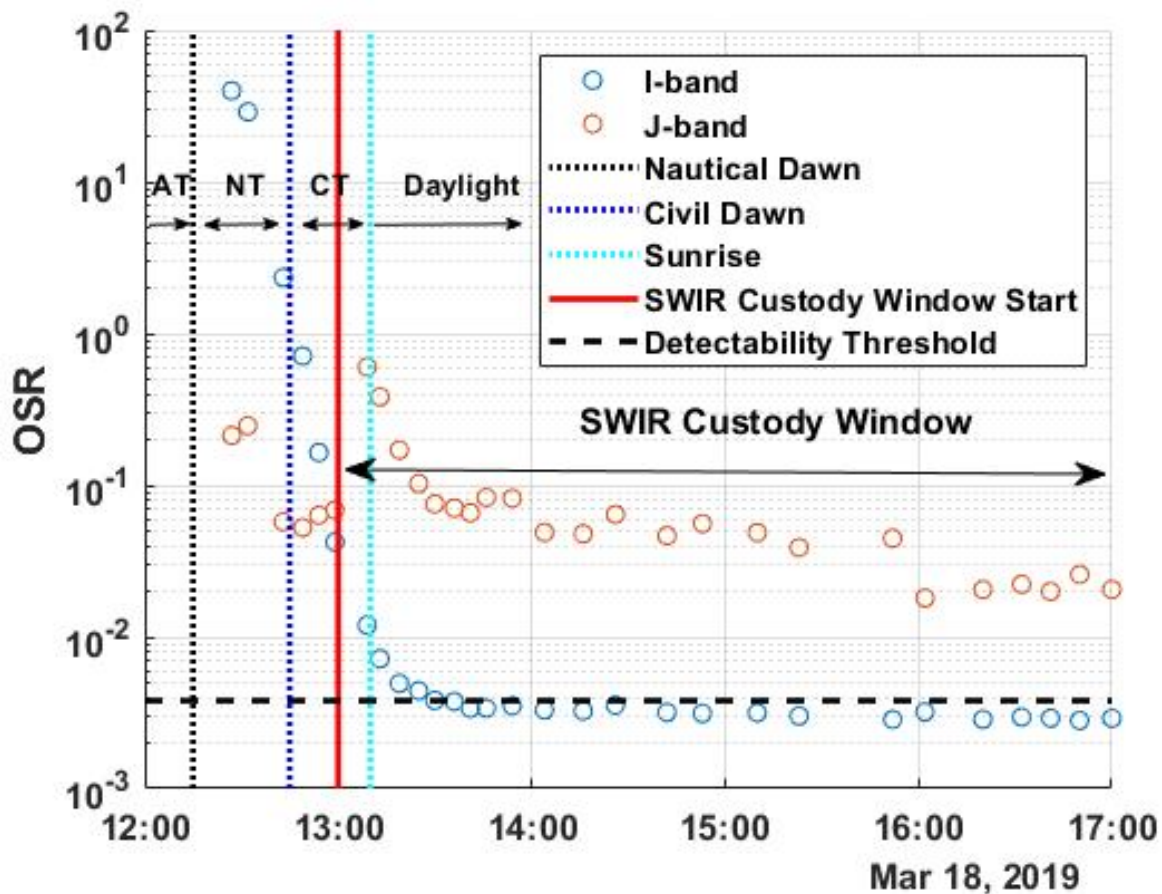


Figure 5: I- and J-band OSRs for the 18 Mar 19, HIP 16489 observations from 1230 – 1700 UTC (0630L – 1100L) from the SOR at Kirtland AFB, NM. The observation azimuths ranged from 2-6° N and elevations of 30-34° measured from the local horizon during the observation period. HIP 16489 catalog fluxes are: 4.72 (I-band) and 4.13 (J-band) [14]. I-band OSRs detectability threshold was observed to be 0.0032 at 1330 (0730L) from Figure 4. The SWIR custody window begins at 1300 UTC for this object (approximately 10 min before sunrise). AT: astronomical twilight; NT: nautical twilight; CT: civil twilight

2.2 Measurement to Photons

Using a Planck function for a 0 visual magnitude, A0 class star (10800K), the flux density arriving at the top of the atmosphere, P , is calculated for each λ within each band. The total photons per second for a given spectral bandwidth, n_{total} , is the sum of all photons within the band accounting for transmission losses, τ_λ , and sensor spectral responsivity losses, QE_λ , given the respective bandwidth, $d\lambda$ and the area of the telescope aperture, πr^2 . This relationship is given in Equation 2. Since the bandwidths of interest are relatively narrow compared to the total overall detector sensitivity, the spectral response was assumed to be constant across each respective band. Sensor spectral responsivities of 0.4 and 0.81 were used for the Rolera and Xenics cameras respectively [12], [21].

$$n_{total} = \sum_{bandwidth} (P_\lambda \tau_\lambda QE_\lambda) d\lambda \pi r^2 \quad (2)$$

The estimated counts per second, n_{cps} , of a 0 visual magnitude, A0 class star (10800K) is shown in Equation 3. A is the band representation of either A_i or A_j as required.

$$n_{cps} = 10^{0.4A} \quad (3)$$

Thus, the photons per count, n_{ppc} , is the ratio of photons per second, n_{total} , to the counts per second, n_{cps} , shown in Equation 4.

$$n_{ppc} = \frac{n_{total}}{n_{cps}} = \frac{\sum (P_\lambda T x_\lambda QE_\lambda) d\lambda \pi r^2}{10^{0.4A}} = \frac{photons/sec}{counts/sec} = \frac{photons}{count} \quad (4)$$

The total counts from each direct sky-radiance measurement image, n_{cpIm} , may then be converted to an estimated photon flux, Φ_{image} using Equation 5.

$$\Phi_{image} = n_{cpIm} \cdot n_{ppc} \quad (5)$$

2.3 LEEDR Model to Photons

LEEDR radiances may be converted to photons for direct comparison to measured flux through a series of conversions. First, the energy per photon is calculated in each band via Equation 6.

$$E_p = \frac{hc}{\lambda} \quad (6)$$

LEEDR simulates the atmospheric conditions (including molecular and aerosol scattering and absorption), Sun position, and look angles. Band-integrated radiances, shown as L_{LEEDR} in units of $W/cm^2 sr$ may then be multiplied by the area of the telescope aperture, $A_{aperture}$, the steradian field of view of the sensor, FOV_{sensor} , and the sensor-specific spectral response, QE_{sensor} . The equivalent photon flux from each LEEDR calculated radiance, Φ_{LEEDR} may be calculated using Equation 7.

$$\Phi_{LEEDR} = L_{LEEDR} \cdot (1/E_p) \cdot A_{aperture} \cdot FOV_{sensor} \cdot QE_{sensor} \quad (7)$$

Cloud contributions to sky radiances were considered to be negligible during each observation/modeling window. However, weather observations from near the Albuquerque Sunport, KABQ, indicate the sky was not completely clear during the observation/modeling time period near 1700 UTC with a few passing clouds occurring as shown in Figure 6. Clouds near the FOV could affect the overall radiance received in the telescope aperture. Future work may consider the effects of clouds on the radiative transfer as other research has successfully demonstrated the efficacy of a systems capable of examining the complex interactions of clouds and atmospheric conditions and their effects on remote sensing systems [5].

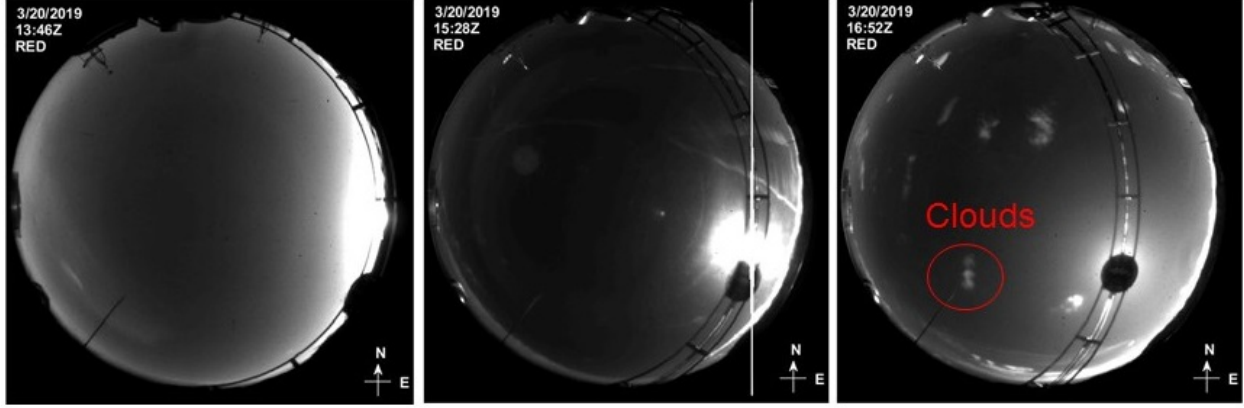


Figure 6: All-sky image taken near SOR on 20 Mar 19 at approximately 1345 (Left) (Sunrise), 1530 (Center) and 1700 UTC (Right). Passing clouds are present especially in 1700 UTC image (Right). Cloud presence near 1700 UTC, particularly in southwest sky near telescope measurement FOV, increases the overall radiance received at telescope aperture.

3 RESULTS

3.0.1 Sky Background Threshold Calculation

From observation of the images in Figure 4, the detectability threshold in the I-band for HIP 16489 occurs near 1330 UTC and was observed to be 0.0032. Since the star is at a near constant flux, the limiting factor in detectability occurs from the increasing radiance of the sky background. The mean I-band sky radiance at 1330 is $3E6$ ADUs. To estimate the correlated equivalent radiance to I-band mean sky background of $3E6$ ADUs, the photon flux of sky background may be equated to the LEEDR derived radiant flux, thus $\Phi_{image} = \Phi_{LEEDR}$. To calculate the total number of instrument counts in an image with a mean background intensity of $S_{meanSky}$ in ADUs, a summation is calculated across all pixels. Vignetting effects were present in the measurement images reducing the total instrument count by a factor of 0.6 by inspection for I-band images. By rearranging Equations 5 and 7, the threshold radiance, $L_{threshold}$, may be calculated using Equation 8.

$$L_{threshold} = \frac{(\sum_{pixels} S_{mean.sky}) \cdot E_p \cdot n_{ppc} \cdot vignetting}{Aperture \cdot FOV_{sensor} \cdot QE_{sensor}} \quad (8)$$

Using Equation 8, a mean I-band sky brightness correlates to a $0.00157 \text{ W/cm}^2 \mu\text{m sr}$ threshold radiance value at the I-band center wavelength ($0.8 \mu\text{m}$). The mean OSR after 1330 UTC is 0.0032 for the I-band and 0.0473 in the J-band. Thus, for this object, there is a 14x improvement in daytime sky OSR on average for the J- as compared to the I-band at this observation elevation and location for the majority of the SWIR custody window.

3.0.2 Analysis of Sky Background Radiance for Daytime Custody

To extend the results of Section 3.0.1 into a more generalized daytime custody scenario, it is necessary to determine the anticipated length of time that the background sky radiance remains at or above the threshold value. This period of increased detectability in the SWIR bands as compared to the NIR band, is referred to as the SWIR custody window. From Section 3.0.1, the SWIR window for a 4.72 VM star at 32° elevation begins during civil twilight for the SOR on 18 Mar 19. Since the Sun's position in the local sky is the primary driver of background sky radiance, we can assume that a similar SWIR-window exists from dawn civil twilight to dusk civil twilight for other dates and latitudes. Thus, the SWIR window, d_{SWIR} , may be estimated for other dates and latitudes using Equations 9 - 12 [16]. Assuming n is the number of days since the vernal equinox (21 March), the declination of the Sun, δ_{Sun} , may be approximated by Equation 9.

$$\delta_{Sun} = 23.5^\circ \cdot \sin \frac{n}{365} \cdot 360^\circ \quad (9)$$

The angle-hour time before solar culmination, τ , may be calculated using, ϕ , the geographic latitude of the observer in Equation 10.

$$\tau = -\tan \phi \cdot \tan \delta_{sun} \quad (10)$$

Since solar culmination occurs at mid-day, the day length, d_l , may be calculated using Equation 11 assuming a τ of 360° is equivalent to 24 hrs.

$$d_l = 2 \cdot \left(\tau \cdot \frac{24hrs}{360^\circ} \right) \quad (11)$$

From the observations of Figure 4, 10 mins of improved twilight detection, d_t , may be added to each side of the day length, d_l , to determine the total SWIR window for a given latitude as in Equation 12. Figure 7 estimates the hours of increased SWIR detection by latitude and time of year. Notably, the SWIR window estimates shown in Figure 7 are for a 4.72 VM object at $4^\circ N$ azimuth and 32° elevation.

$$d_{SWIR} = (2 \cdot d_t) + d_l \quad (12)$$

Figure 7 estimates that a SWIR capable daytime custody sensor, such as the J-band sensor for the observations of Figure 5, would have the 14x increase in observed OSR for 518 hrs. per day based on ground site latitude and time of year.

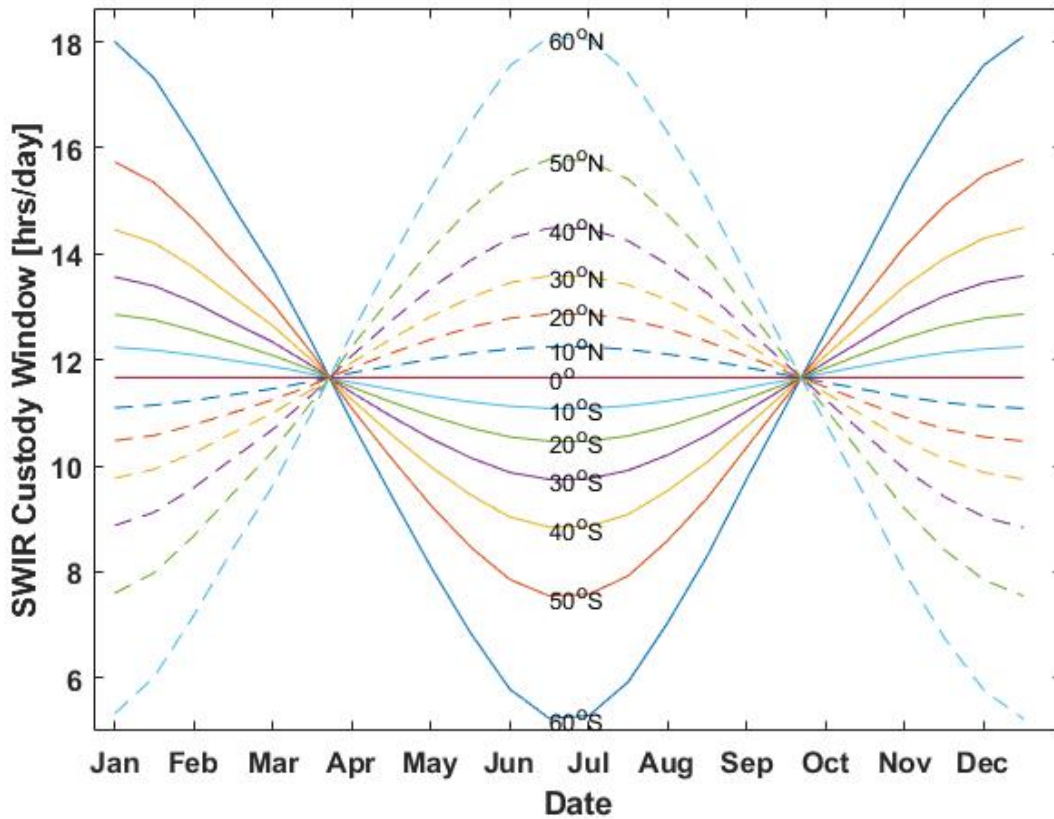


Figure 7: Hours of SWIR custody by latitude for 4.72 VM (I-band) object.

The daytime sky background radiance, however, is not constant. LEEDR has been shown to estimate the sky background radiance in cloudless skies within one order of magnitude. An example of such a model is shown for the Starfire Optical Range for sunrise and local noon in the I-band (Figure 8) and J-band (Figure 9) for 18 Mar 19 using the ExPERT database. The GEO-belt is shown on Figure 8 and 9 for reference.

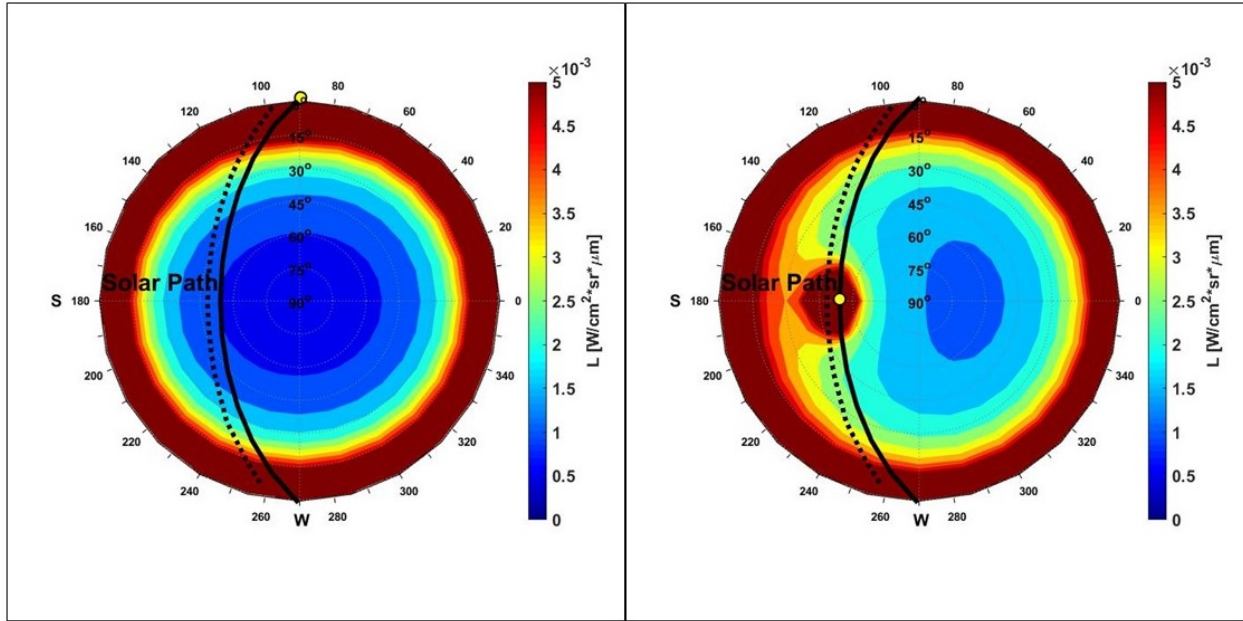


Figure 8: I-band all-sky radiance models for 18 Mar 2019 for the SOR in Albuquerque, NM from LEEDR using ExPERT historical data and a GADS default aerosol profile. Sunrise, 1310 UTC (Left) and solar noon, 1916 UTC (Right). HIP 16489 (I-band flux of 4.72 VM) had an observed detectability threshold of 0.00157 $W/cm^2 \mu m$ sr mean I-band sky brightness wherein higher OSRs were observed in J-band during simultaneous imaging. The solar path is shown as a solid black line, and the GEO-belt is represented by the dotted line as a point of reference. Radiance values exceeding the colorbar scaling are shown equivalent to the maximum scale value.

3.1 Comparing Stars to Satellites

Thus far, the “object” in the object-to-sky has been a star which has the advantage of near-constant flux within the spectral band. While useful for demonstration, reflected signals from Earth-orbiting satellites are seldom constant. Reflected signals depend on solar phase angle, geometry, size, pose, and material reflectance [18]. Most low-Earth-orbiting (LEO) satellites are $\sim 4\text{-}6$ VM and thus the analysis of HIP 16489 may be used as a close proxy for a bright LEO satellite [15], [6], and [11].

3.1.1 LEO Satellites

As the Sun rises and the sky background radiance increases the improved detectability in the J- band over the I-band becomes apparent as shown in Figure 10. Figure 10 shows sample I- and J-band images of a Chinese rocket body CZ-2C R/B (NORAD 31114) in LEO orbit were observed on 20 Mar 19 at 1613 UTC, 324.9° azimuth and 40.8° elevation. At nearly 4 hrs post-sunrise, the sky background in the I-band is noticeably brighter than that of the J-band resulting in a lower OSR and increased difficulty in satisfying the custody mission.

4 CONCLUSIONS

Conventional telescopes equipped with SWIR sensors are a low-cost method of increasing both the quality and quantity of daytime SSA. This research demonstrates the utility of an InGaAs SWIR sensor in terms of increasing the OSR for a group of images during the day. Persistent observation of HIP 16489 demonstrates the benefit to J-band imaging with high OSR after a threshold mean-sky brightness was exceeded. In this instance, at the SOR and observing HIP 16489 target, the detection threshold radiance was exceeded during

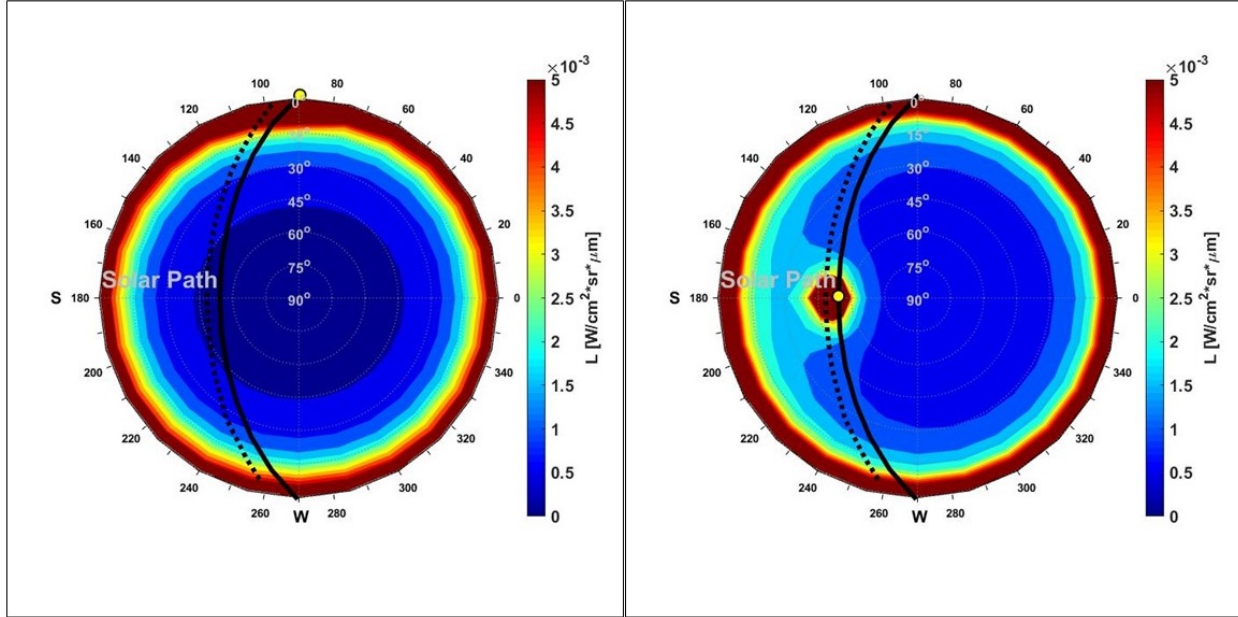


Figure 9: J-band all-sky radiance models for 18 Mar 2019 for the SOR in Albuquerque, NM from LEEDR using ExPERT historical data and a GADS default aerosol profile. Sunrise, 1310 UTC (Left) and solar noon, 1916 UTC (Right). The solar path is shown as a solid black line, and the GEO-belt is represented by the dotted line as a point of reference. Radiance values exceeding the colorbar scaling are shown equivalent to the maximum scale value.

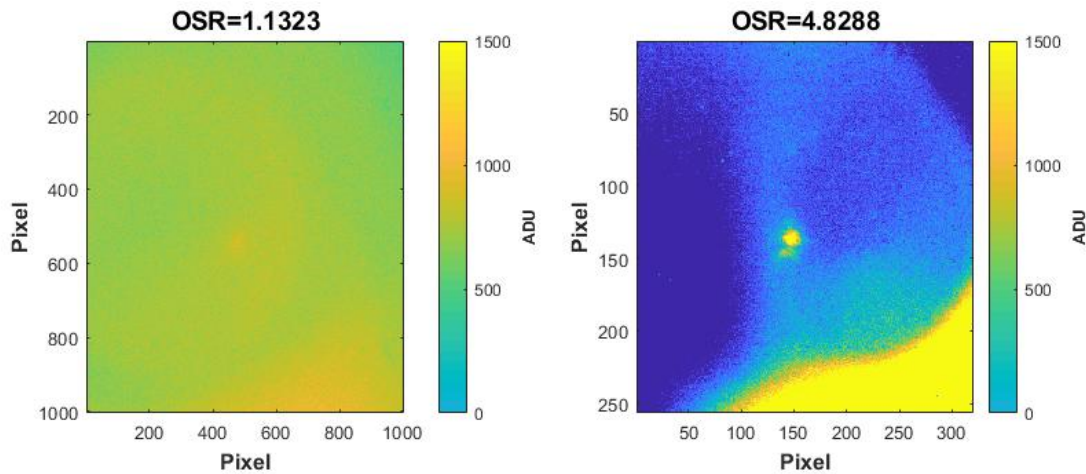


Figure 10: Background-subtracted images of Chinese rocket body CZ-2C R/B (NORAD 31114) in LEO orbit on 20 Mar 19 at 1613 UTC, 324.9° azimuth and 40.8° elevation. I-band image (Left) has significantly lower OSR than J-band image (Right) of orbiting satellite. Images were not over-saturated, scaling was fixed for visualization where pixel values at or above the maximum ADU value are shown in bright yellow.

civil twilight on 18 Mar 19 approximately 45min before sunrise. The mean sky radiance in both the I- and J-bands for sunrise and local noon are shown for the SOR in Figures 8 and 9.

LEO satellites, have observed photometric intensities that fluctuate with size, solar phase angle, satellite pose, and material properties. However, this research shows that HIP 16489, and the CZ-2C R/B are observed with similar I- and J- band sky-to-background detectability ratios in the daytime sky. Post-nautical twilight, appreciable increases in OSR for the J-band image as compared to the I-band was observed for the CZ-2C

R/B. Increasing sky background radiance in the I-band contributes to reduced visibility of the spacecraft which may lead to mis-identification or reduced accuracy in orbit determination methods. Even though the signals from the respective LEO satellites are not constant, this result supports the analysis of HIP 16489 observations that transferring custody from I- band (NIR) to J-band (SWIR) sensors should occur post-nautical twilight to maximize the OSR detectability of satellite targets in the bands-of-interest.

Increased sky radiance contributes to reduced OSR which leads to diminished SSA. Although not comprehensive in the strictest sense, this research is valuable in quantifying the spectral advantages of J-band (SWIR) vs. I-band (NIR) imaging as well as the effects of daytime sky brightness on the greater SSA mission. Comprehensive statistical analysis should consider other stellar targets for persistent observation and analysis including more LEO targets, GEO targets, and dimmer stars. However, this current research provides sufficient evidence to model custody gap trends in the I- and J- bands with reasonable fidelity. The results of this analysis are used to support answers to the research questions posed in RQ2.

I- and J-band is SWIR measurements were taken of the daytime sky and various satellites. Since sky background radiance is the dominant signal (albeit unwanted) for daytime imaging, understanding the effect of spectral sky-brightness on daytime custody is critical. As the sky radiance increases, the J-band sensor begins to outperform the I-band sensor. This crossover occurs at the detectability threshold, where increased signal-to-background ratios were observed in the J-band. Once the magnitude of background sky radiance for the detectability threshold is calculated, LEEDR models of sky radiance were used to determine the spatial and temporal increases in detectability. This research predicted the sky background radiances using the LEEDR atmospheric model. The effect of increasing sky radiance on persistent imaging of an overhead star in the SWIR was shown. A star was chosen as an initial target as it has the advantage of a near constant flux arriving to the sensor. As a follow-on project, LEO satellites, which have observed photometric intensities that fluctuate with size, solar phase angle, satellite pose, and material properties, may be observed with similar I- and J- band sky-to-background detectability ratios in the daytime sky. Thus, from observations of stars, transferring custody from I- band (NIR) to J-band (SWIR) sensors should occur during nautical twilight to maximize the detectability of satellite targets of between 4-6 apparent visual magnitude in the bands-of-interest.

ACKNOWLEDGMENTS

The authors would like to thank the Starfire Optical Range at the Air Force Research Laboratories, Kirtland AFB NM for use of their facilities and assistance in data collection for this project. Data used to generate figures and tables is approved for public release with unlimited distribution by contacting the Center for Space Research and Assurance and Center for Directed Energy at the Air Force Institute of Technology.

REFERENCES

- [1] Ely E. Bell et al. "Spectral-Radiance of Sky and Terrain at Wavelengths between 1 and 20 Microns. II. Sky Measurements". In: *Optical Society of America* 50.12 (1960), pp. 1313–1320.
- [2] A Berk, L S Bernstein, and D C Robertson. *MODTRAN: A Moderate Resolution Model for LOW-TRAN*. Tech. rep. Hanscom AFB, MA: Air Force Geophysics Laboratory, 1987.
- [3] A. Berk et al. *MODTRAN radiative transfer code*. http://modtran.spectral.com/modtran_about. 2014. DOI: 10.1117/12.2050433.
- [4] Jarred L. Burley et al. "A fast two-stream-like multiple-scattering method for atmospheric characterization and radiative transfer". In: *Journal of Applied Meteorology and Climatology* (2017). ISSN: 15588432. DOI: 10.1175/JAMC-D-17-0044.1.
- [5] J. Burley et al. "A Remote Sensing and Atmospheric Correction Method for Assessing Multispectral Radiative Transfer Through Realistic Atmospheres and Clouds". In: *Journal of Atmospheric and Oceanic Technology* 36.2 (2019), pp. 203–216. DOI: 10.1175/JTECH-D-18-0078.1.
- [6] R. Cognion. "Large Phase Angle Observations of GEO Satellites". In: *Society of Photo-Optical Instrumentation Engineers: Defense, Security, and Sensing*. Vol. 8739. 10. 2013. DOI: 10.1117/12.2014623.
- [7] D. Courtney. *What's the Use? V and V of an Atmospheric Characterization and Radiative Transfer Code presentation*. ASME Verification and Validation Symposium, 2015.

- [8] R. Cutri et al. “VizieR Online Data Catalog: 2MASS All-Sky Catalog of Point Sources (Cutri+ 2003)”. In: *VizieR Online Data Catalog* (2003), pp. II/246. URL: <https://ui.adsabs.harvard.edu/abs/2003yCat.2246....0C>.
- [9] Michael T. Eismann. *Hyperspectral Remote Sensing*. (1st). Bellingham, WA: SPIE Press, 2012, p. 748. ISBN: 9780819487889. DOI: 10.1117/3.899758.
- [10] Steven T. Fiorino et al. “Validation of a UV-to-RF high-spectral-resolution atmospheric boundary layer characterization tool”. In: *Journal of Applied Meteorology and Climatology* (2014). ISSN: 15588424. DOI: 10.1175/JAMC-D-13-036.1.
- [11] Michael Hawks. *Telescope Trades AFIT Internal Report*. Tech. rep. Air Force Institute of Technology, 2019.
- [12] Helmut Herrmann and Herbert Bucksch. *Q-Imaging Rolera EM-C² Product Datasheet*. Tech. rep. Mar. 2015, pp. 205–205. DOI: 10.1007/978-3-642-41714-6_{_}31066.
- [13] E. Hog et al. “The Tycho-2 Catalogue of the 2.5 Million Brightest Stars”. In: *Astronomy and Astrophysics* 355 (2000), pp. L27–L30.
- [14] F. van Leeuwen. “Validation of the New Hipparcos Reduction”. In: *Astronomy and Astrophysics* 474.2 (2007), pp. 653–664.
- [15] Tim McLaughlin, Jody Mandeville, and Chris Randell. “Daytime Tracking of LEO Satellites Using Small Telescope Equipped with COTS SWIR Camera Presentation”. In: *Small Telescope Workshop*. Chantilly, 2019.
- [16] Jean Meeus. *Astronomical Algorithms*. (2nd). 804. Richmond, VA: Willmann-Bell, Inc., 1998, pp. 101–104. URL: www.willbell.com.
- [17] Gerald Persha. *Cousins/Bessell vs. Johnson Filter Standards*. Tech. rep. Optec, Inc., 1999. URL: <http://www.optecinc.com/astronomy/products/filtmono.html>.
- [18] Grant Thomas et al. “Daytime SNR modeling of GEOs in the SWIR for low-cost, ground-based imaging”. In: *Advanced Maui Optical and Space Surveillance Technologies Conference (AMOS)*. 2018.
- [19] K. Tohsing et al. “Validation of Spectral Sky Radiance Derived from All-Sky Camera Images - A Case Study”. In: *Atmospheric Measurement Techniques* (2014). ISSN: 18678548. DOI: 10.5194/amt-7-2137-2014.
- [20] Nathan P. Wurst, Joseph Meola, and Steven T. Fiorino. “Improved atmospheric characterization for hyperspectral exploitation”. In: *Society of Photo-Optical Instrumentation Engineers: Defense + Security Proceedings* (2017). DOI: 10.1117/12.2265853.
- [21] *Xenics Xeva-1.7-320 Product Datasheet*. Tech. rep. Leuven, 2019. URL: www.sinfrared.com.
- [22] Giuseppe Zibordi and Kenneth Voss. “Geometrical and Spectral Distribution of Sky Radiance: Comparison between Simulations and Field Measurements”. In: *Remote Sensing and Environment Journal* 27 (1989), pp. 343–358.